Evaluation of soil-geogrid interaction using transparent soil with laser illumination

X. Peng[1] and J. G. Zornberg[2]

[1]*Former PhD student, Department of Civil, Architectural, and Environmental Engineering, University of Texas at Austin, Austin, TX 78712, USA, E-mail: xin_peng@outlook.com*
[2]*Professor, Department of Civil, Architectural, and Environmental Engineering, University of Texas at Austin, Austin, TX 78712, USA, E-mail: zornberg@mail.utexas.edu (corresponding author)*

Received 30 June 2018, revised 15 October 2018, accepted 02 December 2018

ABSTRACT: An experimental methodology was developed involving techniques that allow non-intrusive measurement of confined geogrid deformations and soil particle displacements under pullout loading condition, which together are expected to generate a comprehensive volume of data including the entire displacement field in both geogrid and surrounding soil. The techniques involve the use of transparent soil with laser-aided imaging, which allows visualization and facilitates subsequent evaluation of the load-transfer mechanisms that develop between soil particles and the different rib elements in geogrids. A laser beam was employed to track the transparent soil particles in a plane perpendicular to the soil-geogrid interface. The collimated laser beam produced well-defined individual particles in the selected plane of the soil model. Digital cameras were used to track the displacement fields of both the confined geogrid specimen and soil particles within the laser-illuminated plane. Digital image correlation as well as other image-processing techniques were used to define the displacement fields based on images captured during the tests. The field displacements resulting after processing the data gathered from the newly developed experimental system led to well defined manifestations of the load transfer mechanisms, including the deflection patterns in geogrid ribs and shear bands within the soil mass.

KEYWORDS: Geosynthetics, Soil-geogrid interaction, Transparent soil, Laser illumination, Digital image correlation, Shear band

REFERENCE: Peng, X. and Zornberg, J. G. (2019). Evaluation of soil-geogrid interaction using transparent soil with laser illumination. *Geosynthetics International*, **26**, No. 2, 206–221. [https://doi.org/10.1680/jgein.19.00004]

1. INTRODUCTION

While introduced reasonably recently into the portfolio of geotechnical materials, geogrids are now extensively used to enhance the performance of embankments, walls, and roadways. They were first used in the UK in 1980 and have been subsequently used extensively in North America since 1982 (Koerner 2012). The rise in geogrid use in retaining walls and roadways was triggered by several factors, including: (1) good quality control in the manufacturing process; (2) expeditious and easy installation; (3) economic benefits, compared to alternatives involving traditional construction materials; and (4) good performance under static and seismic conditions in a growing range of civil engineering applications.

Traditional design methods for geogrid-reinforced soil retaining structures have typically been based on the evaluation of the ultimate (failure) condition using techniques such as limit-equilibrium. On the other hand, typical design approaches for geogrid-stiffened roadway systems have been based on serviceability considerations that involve predicting levels of deformation and distress using semi-empirical methods. The design of geotechnical systems involving geosynthetics under either ultimate or serviceability considerations require quantification of the mechanical properties governing the soil-geosynthetic interface. This includes parameters to quantify the interface shear strength or the stiffness of the soil-geosynthetic composite, depending on the design criteria for the ultimate or serviceability states, respectively. The actual soil-geogrid interaction behavior under service conditions would particularly benefit from proper evaluation of the load-transfer mechanisms between soil particles and reinforcement. In the past two decades, a number of studies have been conducted to assess these mechanisms, including experimental testing programs (Ochiai *et al*. 1996; Alagiyawanna *et al*. 2001; Ziegler and Timmers 2004; Teixeira *et al*. 2007; Sieira *et al*. 2009;

Bathurst and Ezzein 2016, 2017; Wang *et al*. 2016; Roodi and Zornberg 2017) and numerical investigations (Wilson-Fahmy and Koerner 1993; Tran *et al*. 2013; Wang *et al*. 2016), all of which focused on the load transfer behavior of geogrids with rectangular apertures. While the previous studies have provided good insight into the response of geogrids under specific load conditions, no focus has been placed on the measurement of geogrid rib deflection and displacement of soil particles induced by geogrid movement. This is understandable, given that most conventional tests only allow measurement of geogrid junction displacements at limited locations and no measurement of rib deflection and soil particle movement. One of the applications where additional insight into the measurement of rib deflection and soil particle displacement would be particularly relevant is in relation to applications involving roadway stabilization. In this case, the improved stiffness behavior of geogrid-stabilized base layers has been evaluated via laboratory and field tests (Collin, Kinney, and Fu 1996; Chen, Abu-Farsakh, and Tao 2009; Abu-Farsakh and Chen 2011). However, the load transfer mechanisms between soil particles and geogrid specimens are still not understood sufficiently to explain the increased stiffness exhibited by the soil-geogrid composite layer.

Over the past decade, image-based techniques have been used extensively to measure deformation fields in geotechnical laboratory model tests (Zornberg *et al*. 1998; Otani *et al*. 2000; White *et al*. 2003). Digital image correlation (DIC, also called particle image velocimetry/PIV in experimental fluid mechanics) is an automatic target tracking method that has been implemented to evaluate the movement of regular soil particles (White 2002). Transparent soils, such as those containing amorphous silica materials and pore fluids with a matching refractive index, have recently been utilized to understand the behavior of geotechnical systems (Iskander 2010; Ezzein and Bathurst 2014; Black 2015; Chini *et al*. 2015; Ferreira and Zornberg 2015). In these investigations, continuous spatial deformations within the soil mass could be measured using digital cameras and image processing techniques, such as DIC, without causing the physical disturbances that often occur with sensor measurements. Specifically, in studies of soil-geogrid interaction using transparent soil, Ezzein and Bathurst (2014) and Ferreira and Zornberg (2015) placed multiple painted soil particles near the soil-geogrid interface to track particle displacements. Several differences have been identified between the study conducted by Ezzein and Bathurst (2014) and the study presented in this paper. Specifically, different pullout box dimensions were used: the former study used a large-scale pullout box, whereas this study involved a small-scale pullout box that allowed use of techniques such as laser illumination. In addition, because of the different pullout box scales, different reinforcement specimen sizes were adopted: a comparatively larger testing setup and reinforcement specimens facilitate a more realistic simulation of field cases, but a reduced scale approach facilitates obtaining high-resolution measurements of individual rib elements and soil displacement profiles. Also, the tests reported by Ezzein and Bathurst (2014) involved applying a constant loading rate to a clamp placed within the confined soil mass to minimize the potential boundary effect at the frontal wall. On the other hand, comparatively short reinforcement specimens in the smaller scale tests are typically more sensitive to the potential disturbance from the movement of the confined clamp system with net load correction; consequently, in this study, a constant displacement rate was applied to the roller grip to which the unconfined portion of the geogrid specimen was attached via a clamping system. An additional difference is that the rear end of the confined reinforcement was clamped in the study conducted by Ezzein and Bathurst (2014) to simulate field situations, although this prevents pullout failure. Instead, the rear end of the geogrid specimen in this study was only confined by soil particles and consequently the total force recorded at the top front equals the total resistance contribution from rib elements. Finally, Ezzein and Bathurst (2014) adopted the use of painted particles to track soil particle displacements, whereas a laser system was adopted in this study to illuminate the soil displacement at a given plane, which was relatively close to the center portion of the pullout box. Overall, the differences between these two studies are expected to lead to complementary observations and conclusions. In other geotechnical applications of transparent soil, the use of laser techniques proved to be particularly useful to investigate the entire field of soil particle displacement. This includes the studies conducted by Iskander (2010), who used laser light to visualize particle displacements beneath a model footing during load tests, research reported by Black (2015), who implemented a laser-aided system to track the particle displacements in centrifuge tests, and the work by Chini *et al*. (2015), who applied laser light to visualize shear failure surfaces induced by several types of in-situ undrained loading in transparent clay.

Unlike other planar geosynthetics, geogrids develop a soil-interlocking interaction that leads to the mobilization of different types of resistance from different rib elements. The resistance mobilized by the different rib elements ultimately determines (1) the ultimate pullout resistance, and (2) the confined stiffness of the soil-geogrid composite. Deformations of the different rib elements, particularly of bearing rib elements, have been difficult to quantify using conventional experimental techniques. Significant insight has been provided by previous researchers (e.g. Wilson-Fahmy and Koerner 1993; Ochiai *et al*. 1996; Ziegler and Timmers 2004; Teixeira *et al*. 2007; Ferreira and Zornberg 2015; Bathurst and Ezzein 2016) to quantify the resistance from bearing elements of geogrids during the pullout process. However, these evaluations typically involved empirical correlations or indirect experimental measurements using modified geogrids with some of the bearing elements removed. In this study, the deflection profiles of the bearing elements of different geogrids could be measured at a comparatively high resolution by adopting the developed experimental techniques. This type of measurement allowed use of

mechanics, such as beam theory, to correlate the deflection measurements to the resistance acting on each bearing element.

The scope of the research component presented in this paper is part of a broader research program conducted by the authors that includes (1) developing a series of experimental techniques using transparent soil to facilitate determination of the displacement fields within both the soil and geogrid for pullout testing conditions; (2) developing load transfer models for geogrids under pullout loading using the measurements obtained from the experimental component; and (3) comprehensively evaluating and comparing the different load transfer mechanisms that develop for geogrids with different geometric characteristics. A preliminary phase in the development of the experimental techniques was previously reported by Peng and Zornberg 2017 and included quantification and evaluation of displacement data within geogrid reinforcements. The current paper expands on the previous work, with emphasis on the advanced experimental techniques now used to quantify the displacement field within the soil mass surrounding a geogrid reinforcement. As will be discussed, this quantification was achieved by incorporating laser-aided imaging and newly adopted image-processing techniques. These new techniques and the corresponding measurements are expected to provide a robust evaluation of load transfer mechanisms between soil and geogrids with different geometric characteristics. Prototype test results obtained in this study aim at defining deflections of bearing rib components in a confined geogrid, which are useful to quantify the relative contribution from those bearing rib components for load levels ranging from working stress conditions to failure. Additionally, soil particle displacements in the direction of loading and shear band mobilization are evaluated for increasing frontal load levels. This information would also facilitate understanding of the load transfer mechanisms between soil and geogrids with different geometric characteristics. Since this paper aims at describing the capabilities of the experimental techniques, only typical results from prototype tests are presented. While the focus of the study conducted by the authors has been on the geometric characteristics of geogrids, it should be noted that the complex load transfer mechanisms between soil particles and geogrids are influenced by a number of additional factors, such as soil particle size and distribution, geogrid material properties, and the experimental configuration. This research program keeps factors other than geometry unchanged and focuses only on the evaluation of this particular effect on load-transfer mechanisms.

2. TEST MATERIALS

2.1. Transparent soil

The solid particles used in this study involved crushed fused quartz, which has been previously described by Ferreira (2013). According to the Unified Soil Classification System (USCS), this material classifies as a poorly graded sand (SP). Selected geotechnical properties of the crushed fused quartz particles are summarized in Table 1. This indicates that the friction angle of the oil-saturated soil obtained from direct shear tests is only one degree lower than that of the dry particles, likely due to the lubrication by the pore fluid.

The pore fluid used in this investigation is a mixture of two clear mineral oils: Puretol 7 and Paraflex HT4 (please see Table 2 for manufacturer names and locations). Puretol 7, and another type of mineral oil, Krystol40, have previously been used by Ezzein and Bathurst (2011, 2014). Due to the unavailability of Krystol40, Paraflex HT4 has been used instead for this study. Selected properties of Puretol 7 and Paraflex HT4 are presented in Table 2. This indicates that Puretol 7 has a higher refractive index (RI) than the solid fused quartz, while Paraflex HT4 has a lower refractive index. Therefore, a specific volume ratio between these two liquids was selected so that the refractive index of the final mixture was targeted to be the same as that of the fused quartz particles. Figure 1 displays a sample of transparent soil confining a biaxial geogrid to illustrate the results obtained after preparing the mix of fluids to match the RI of the crushed fused quartz particles. Approximately the lower two thirds of this soil sample are submerged in the oil mixture, while the top third is in a dry condition.

Table 1. Select geotechnical properties of the crushed fused quartz used in this study

Property	Test method	Value
Specific gravity, 20°C	Water Pycnometer Test (ASTM D854)	2.203
Maximum–index dry density, g/cm^3	Vibratory Table Test (ASTM D4253)	1.336
Minimum–index dry density, g/cm^3	Vibratory Table Test (ASTM D4254)	1.203
Friction angle, dry	Direct Shear Test (ASTM D3080)	45°
Friction angle, oil saturated, drained	Direct Shear Test (ASTM D3080)	44°

Table 2. Select properties of both components of liquid mixture (provided by the manufacturer[a])

Properties	Puretol 7	Paraflex HT4
Density, 15°C, g/cm^3	0.859	0.836
Viscosity, 40°C, cSt	12.2	3.8
Color	Clear and bright	Clear and bright
Odor	No odor/slight petroleum oil-like	Mild petroleum oil-like
Flash point, °C	>170	>125
Pour point, °C	−20	−57
Refractive index, 22°C	1.4635	1.4532
Solubility	Insoluble in water	Insoluble in water
Chemical stability	Stable	Stable
Emergency overview	No specific hazard	No specific hazard

[a]The two mineral oils are Puretol 7 manufactured by Petro-Canada Lubricants Incorporation (Ontario, Canada) and distributed by Coast Southwest Incorporation (Placentia, CA, USA); Paraflex HT4 manufactured by Petro-Canada Lubricants Incorporation and distributed by Schmidt and Sons Incorporation (Dallas, TX, USA).

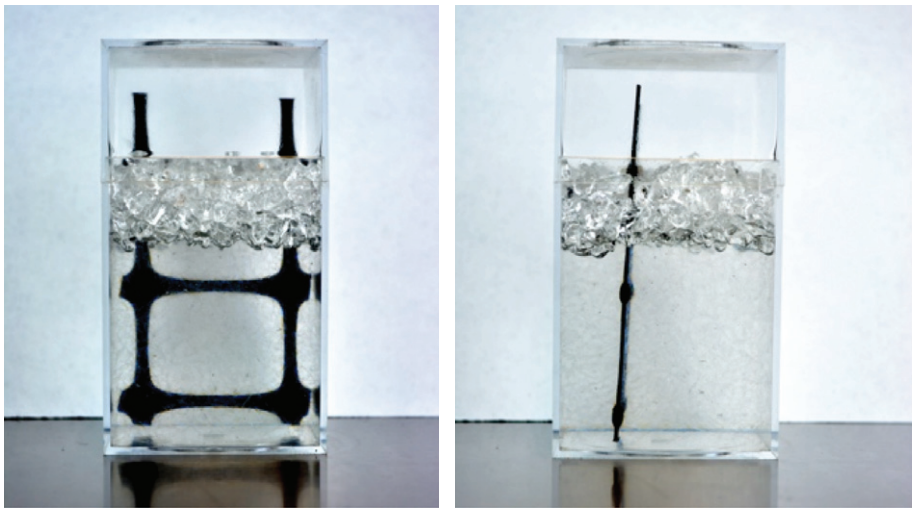

Figure 1. A sample of transparent soil confining a biaxial geogrid: (a) frontal view and (b) side view

Table 3. Nominal geometric characteristics of selected geogrids used in this study (provided by the manufacturer[a])

Geogrid	Aperture shape	Rib	Rib pitch (mm)	Mid-rib depth (mm)	Mid-rib width (mm)
G1	Rectangular	Longitudinal[b]	33	0.76[c]	3.0[c]
		Transverse[b]	25	0.93[c]	3.0[c]
G2	Triangular	Longitudinal[b]	40	1.6	1.3
		Diagonal[b]		2.0	1.0

[a]All geogrids are manufactured by Tensar International Corporation.
[b]The longitudinal direction is along the cross-machine direction, while the transverse direction is along the machine direction.
[c]The manufacturer did not provide the dimensions, therefore, they were determined by the writers according to selected testing specimens.

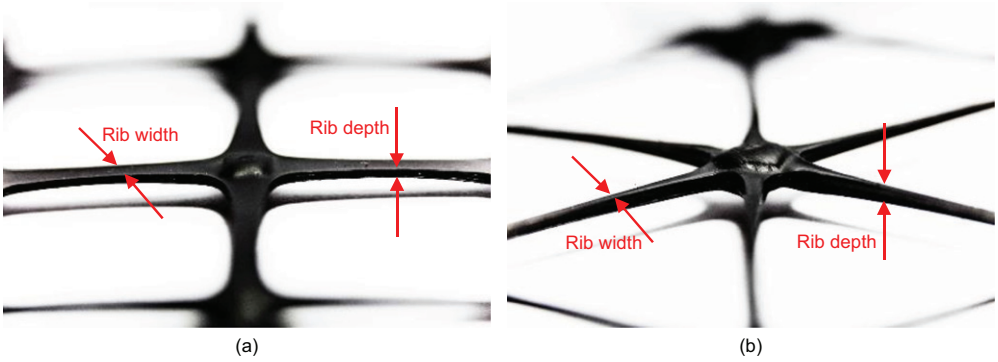

Figure 2. Comparison of junction and rib shapes: (a) Geogrid G1 and (b) Geogrid G2

2.2. Geogrid characteristics

The geogrids evaluated in this study are polypropylene (PP) products manufactured by punching holes in PP sheets, which are then heated and stretched in different directions. This type of geogrid exhibits two common features as a result of the manufacturing process: (1) the dimensions of the rib cross-sections vary along the length of the rib, having the minimum rib depth and width at approximately the mid-length of the rib; and (2) the junction nodes, which are the intersections of different ribs, typically have a greater depth than the rest of the rib sections. Geogrids with two different aperture shapes were evaluated in the experimental tests: (a) biaxial geogrids with rectangular aperture shape; and (b) triaxial geogrids with triangular aperture shape. The entire research program evaluates more than five types of geogrids with different geometric characteristics. Illustrative test results of a portion of this study, involving the use of Geogrids G1 and G2, as well as the corresponding measurement techniques, are reported in this paper. The nominal geometric characteristics of these two geogrids are presented in Table 3. The triangular aperture shape of the triaxial geogrid defines an approximately equilateral triangle. The geometric characteristics of Geogrids G1 and G2 are presented in Figure 2.

In addition to the aperture shapes, three additional characteristics that differ between the biaxial and triaxial geogrids can be observed from Figure 2: (1) the rib widths

of the biaxial geogrid are larger than those of the triaxial geogrid; (2) the rib depths of the triaxial geogrid are larger than those of the biaxial geogrid; and (3) the biaxial geogrid has an orthogonal junction shape, while the triaxial geogrid has a hexagonal junction shape.

3. EXPERIMENTAL SETUP AND MEASURING METHODOLOGY

3.1. Experimental setup

A frontal view of the experimental apparatus developed for this study is illustrated in Figure 3. The loading system and data acquisition system used in this study are based on those reported by Ferreira (2013). The nominal dimensions of the confined portion of the geogrid specimens were 200 mm in width by 230 mm in length. The unconfined portion of the geogrid specimen was attached to a roller grip using a clamping system. The roller grip was connected to a load cell that measured the frontal pullout load during testing, while the other end of the load cell was fixed to the moving head of the load frame, the speed of which was controlled by a load control system. A loading displacement rate of 1 mm/min was applied to the moving head of the load frame during testing. The lengths of the unconfined portion of all geogrid specimens tested were minimized and maintained to be approximately the same among different specimens to reduce the effect of the unconfined tensile behavior on the confined performance of reinforcement.

The loading system used in this study is a universal testing machine composed of a fixed base and moving head, with a maximum load capacity of 267 kN. The load was powered and controlled using National Instruments (Austin, TX, USA) SCXI hardware and LabVIEW software. The load on the moving head was recorded by an S-type load cell with a maximum load capacity of 22 kN.

The transparent soil model prepared as a part of this study followed similar protocols as those reported by Ferreira (2013). The mold was composed of a transparent box with internal dimensions of 300 mm in length, 250 mm in width and 150 mm in depth. The box included a stainless-steel lid with a flexible air bladder. The transparent box was composed of three internal transparent walls (one transparent frontal wall and two transparent sidewalls) made of abrasion-resistant polycarbonate, and an external stainless-steel frame as reinforcement for the walls. A series of screws was fixed to the stainless-steel frame beams for use as reference points to align the sensor planes of the cameras with the tracking planes at both the frontal and side views. The transparent box was fixed to the base of the load frame with six stainless steel screws. The roller grip, transparent box and base of the load frame were aligned with each other to ensure that the geogrid specimen was uniformly loaded in-plane along its width. To avoid oil leakage, the transparent pullout box was sealed using a sealant designed for aircraft sealing applications. A 12.7-mm opening was made in the top wall of the transparent box (see configuration in Figure 3) to extend the geogrid specimen to the outside of the box

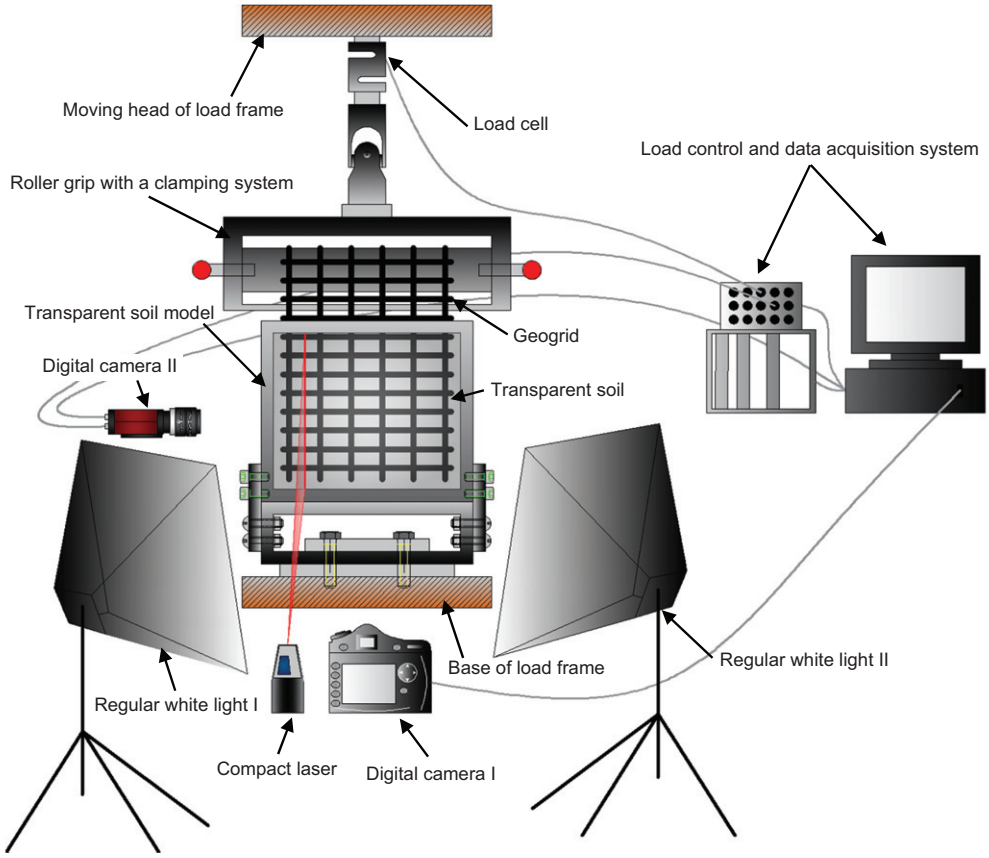

Figure 3. Schematic diagram of frontal view of developed experimental apparatus

for attachment to the roller grip. Two sleeves, extending 15.9 mm into the soil mass in the box, were welded to the borders of this opening to minimize potential boundary effects at the frontal confined boundary. To apply confining pressure, compressed air was delivered through a flexible and oil-resistant rubber bladder attached to the stainless-steel lid and controlled by a pressure regulator with a maximum supply of 3447 KPa. A digital pressure gauge with a range up to 207 KPa and an accuracy of 0.52 KPa was also used to monitor the applied confining pressure during testing.

Load data recording and digital image capturing were controlled and synchronized by the load control and data acquisition system (DAQ) shown in Figure 3. The load data recording frequency was 5 Hz.

A digital camera (Digital Camera I in Figure 3) was used to track geogrid deformations from the frontal view of the transparent soil model. This camera has a 24-megapixel Advanced Photo System type-C (APS-C) sensor with a crop factor of 1.5. Both the camera and the lens used in this study were manufactured by Nikon Inc. (Melville, NY, USA). An APS-C format zoom lens with a focal length ranging from 18 mm to 55 mm was attached to this camera. The average lens distortion (often referred to as TV Distortion) of this lens is less than 0.05% with a focal length greater than 35 mm. In this study, the focal length range of this lens used in this study ranged from 45 to 55 mm. A comparatively large focal length allowed the camera to be positioned relatively far from the geogrid plane, which reduced measurement errors related to out-of-plane motion. Furthermore, only the central areas of the images, which are expected to have less distortion than the edge areas, were used for image analysis. Therefore, the effect of lens distortion on digital image measurement was disregarded in this study. The camera was remotely controlled using the NI DAQ with a LabVIEW programming code provided by Ackermann Automation GmbH (Frankfurt am Main, Germany). The recorded images were transmitted directly from camera to PC via an extended USB cable. A second digital camera (Digital Camera II in Figure 3) was used to track the soil displacement field in the laser-illuminated plane from the side view of the transparent soil model. This camera has a 5-megapixel Type 2/3 sensor with a crop factor of 3.93. A C-Mount lens with a fixed focal length of 16 mm was attached to this camera. The average lens distortion of this lens is reported to be −0.05%. As with the images from Digital Camera I, only the central areas of the images were used for image analysis. The camera was powered and controlled by the DAQ using a LabVIEW programming code, and the triggering signals were transmitted from the DAQ through an I/O cable with a 12-pin Hirose connector. The recorded images were transmitted directly from camera to PC via a Gigabit Ethernet (GigE) cable. The image sampling frequency for both digital cameras was 0.2 Hz. To ensure that the planes of the camera sensors were parallel to the tracking planes, the reference grids in the live view of the cameras were aligned with the reference screws, which were fixed to the stainless-steel frame beams of both frontal and side walls.

After alignment of the planes of the camera sensors to tracking planes was accomplished, the displacements of pixels in the recorded images were converted into physical units (e.g. millimeters) using a calibration box, the details of which were previously discussed by Ferreira (2013).

The regular white lighting system was composed of two 160 W photo studio soft boxes measuring 406 mm in width and 610 mm in length. This provided relatively uniform light on the frontal transparent wall (see configuration in Figure 3) of the transparent soil model, which measured 250 mm in width and 300 mm in length. The light bulbs had a color temperature of 6500 K, which is similar to common daylight. The main purpose of this lighting system was to illuminate the geogrid and capture deformation of its ribs.

The laser system involved two compact lasers, both with a wavelength of 638 nm. One was a single mode laser with a maximum output power of 175 mW, while the other was a multi-mode laser with a maximum output power of 350 mW. Both lasers can generate a vertical line with a fan angle of 30°. The single mode laser provides a ±14% uniformity of intensity distribution along the laser line, with higher power at the ends, while the multi-mode laser provides a ±30% uniformity of intensity distribution along the laser line, also with higher power at the ends. Both lasers offered stable power and temperature to generate a consistent line. Also, both laser units allowed full control of the settings regarding laser power, temperature and variable laser modulation sequence. The lines generated by the two lasers overlapped during testing to maximize the power of the laser-light plane to illuminate particle movement.

Because diffusion of the laser light could contaminate the lighting system for geogrid tracking using Digital Camera I, a 10-s ON-OFF time sequence was implemented for laser shooting. On the other hand, the regular white light source consists of light beams with different wavelengths (e.g. different colors) that were neither coherent nor collimated. These light beams can attenuate the contrast of the fused quartz particle boundaries illuminated by the monochromatic, coherent, collimated red laser light. Consequently, a red filter was attached to the lens of Digital Camera II (Figure 3) to cancel out light beams other than red. Figure 4 displays two images of the transparent soil sample, with and without the red filter, under the lighting system with both white and laser light. In the image captured with the red filter (Figure 4a), the particle boundaries have a starker contrast than those in the image captured without the red filter (Figure 4b).

In Figure 5a, an image is shown of the frontal view of the transparent soil model with a confined geogrid specimen captured by Digital Camera I. An image of the side view of the transparent soil model captured by Digital Camera II during the same test with laser shooting is presented in Figure 5b. In this test, permanent white markers were painted on the top of the geogrid specimen to facilitate the subsequent image analysis via Digital Image Correlation (DIC) techniques. The rib shadows seen on the left in Figure 5b were created by the transverse ribs blocking laser light penetration. The shadows moved upward as the transverse ribs moved during progress

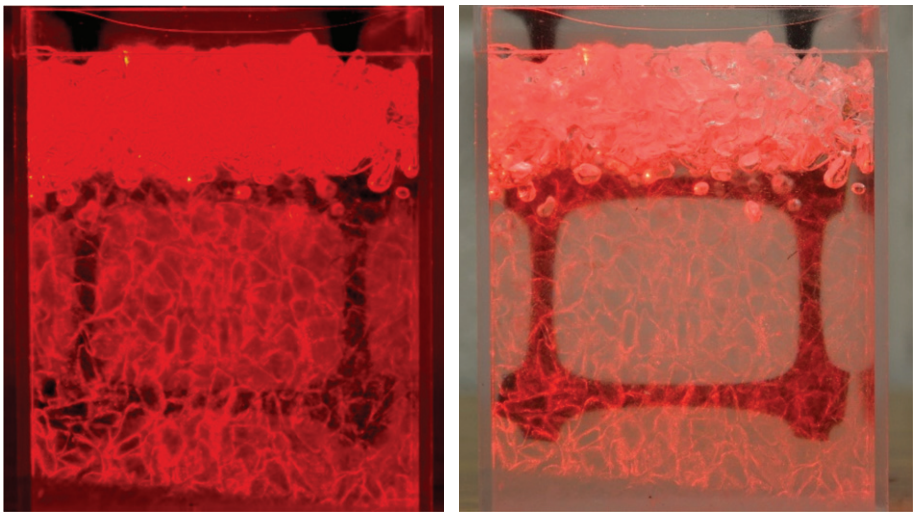

Figure 4. Images of transparent soil sample under light condition with both white light and laser light captured: (a) with red filter and (b) without red filter

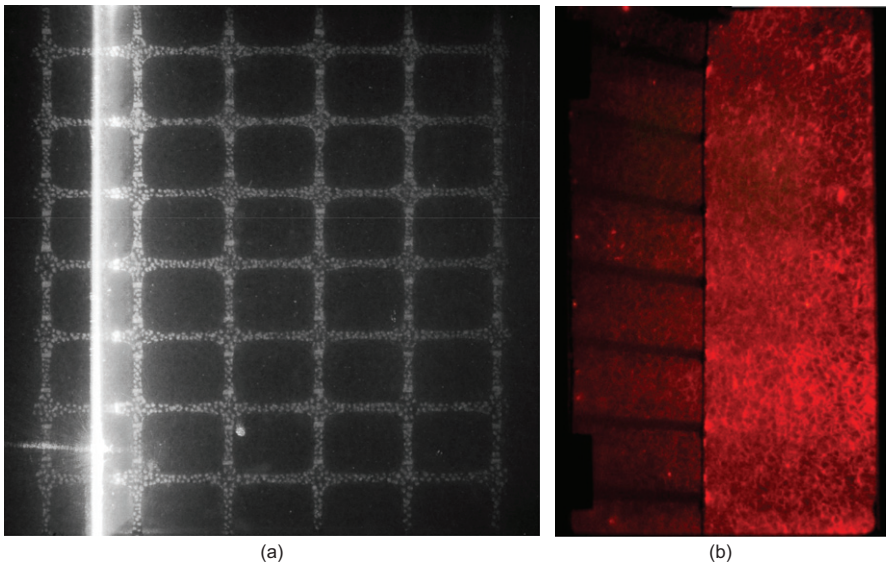

Figure 5. Transparent soil test with a confined geogrid specimen G1: (a) frontal-view image captured by Digital Camera I and (b) side-view image captured by Digital Camera II during laser shooting

of the test. The movements of the shadows could adversely affect the quality of the DIC analysis for tracking the displacement field of fused quartz particles. Consequently, only the area in front of the geogrid specimen (on the right in Figure 5b) was used for soil displacement tracking.

3.2. Image processing techniques

Several image processing techniques were adopted in this study based on aspects such as the geometric characteristics and the range of displacement of the tracked objects, uniformity of light illumination, and image quality. All recorded images were converted to greyscale before conducting further image processing. Multiple tools, including ImageJ (Bethesda, MD, USA), Mathematica (Champaign, IL, USA), MATLAB and Excel, as well as some other open source programming codes, were utilized for image processing and data interpretation.

One of the main displacement tracking methods used in this study was DIC. The DIC code used was an open source MATLAB code developed by Jones (2015) with a resolution of 1/10 of a pixel. To achieve this resolution, nine discrete correlation coefficients surrounding the absolute maximum coefficient are interpolated using a second order polynomial in both the horizontal and vertical directions. In the correlation process, the default reference image is the first image in the current DIC analysis directory. The code also allows use of the preceding image as the reference image, which was found to be useful in cases involving large deformation of the tracking object and/or large distortions of the tracking patterns. However, cumulative errors may also be generated when the cumulative displacements are calculated using preceding images as reference. Therefore, in the analysis conducted in this study, the first image was treated as the

reference image if good correlation results were obtained. The selection of the subset size for image correlation depends on several factors, such as the selected search zone size, estimated maximum movement of tracking features, selected reference image for correlations (either the first image or preceding reference images), and overall image quality. If the first image was selected as the reference image, and the search zone size selected was two times the subset size, the subset size was generally selected as slightly over two times the estimated maximum displacement of tracking feature. However, if the displacement range of the tracking feature varied significantly, size-reduced images may be required to initially estimate the maximum displacement of the tracking features. The precision and accuracy of the DIC code adopted in this study were comprehensively evaluated under different conditions by Jones (2014) using standard test images provided by the Society for Experimental Mechanics (SEM) DIC Challenge. Considering conditions with varying contrast of the tracking patterns, and different displacement, rotation and strain levels, errors of displacement measurement were reported to be from 0.005 to 0.088 pixels with standard deviations from 0.004 to 0.057 pixels. Errors of strain measurement were reported to range from 0.014% to 0.534%, with standard deviations ranging from 0.012% to 0.686%.

The DIC calculations conducted to analyze the results of one of the experimental tests conducted using Geogrid

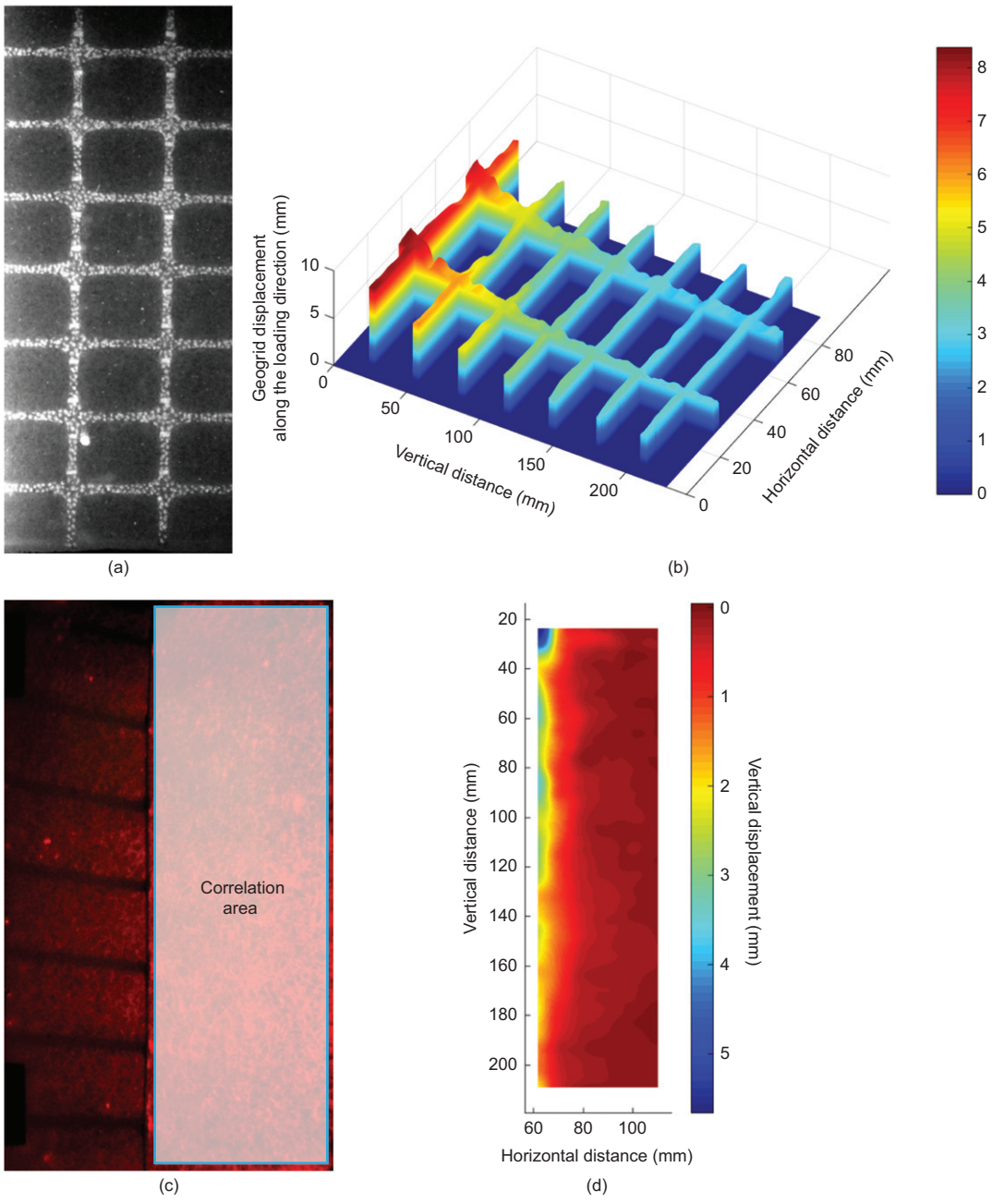

Figure 6. Selected DIC calculation results obtained from the test conducted using Geogrid G1: (a) correlation area in the frontal-view image, and (b) the corresponding vertical displacement field of the geogrid at the time reaching pullout failure; (c) correlation area in the side-view image, and (d) the corresponding vertical displacement field of soil particles at the time reaching pullout failure

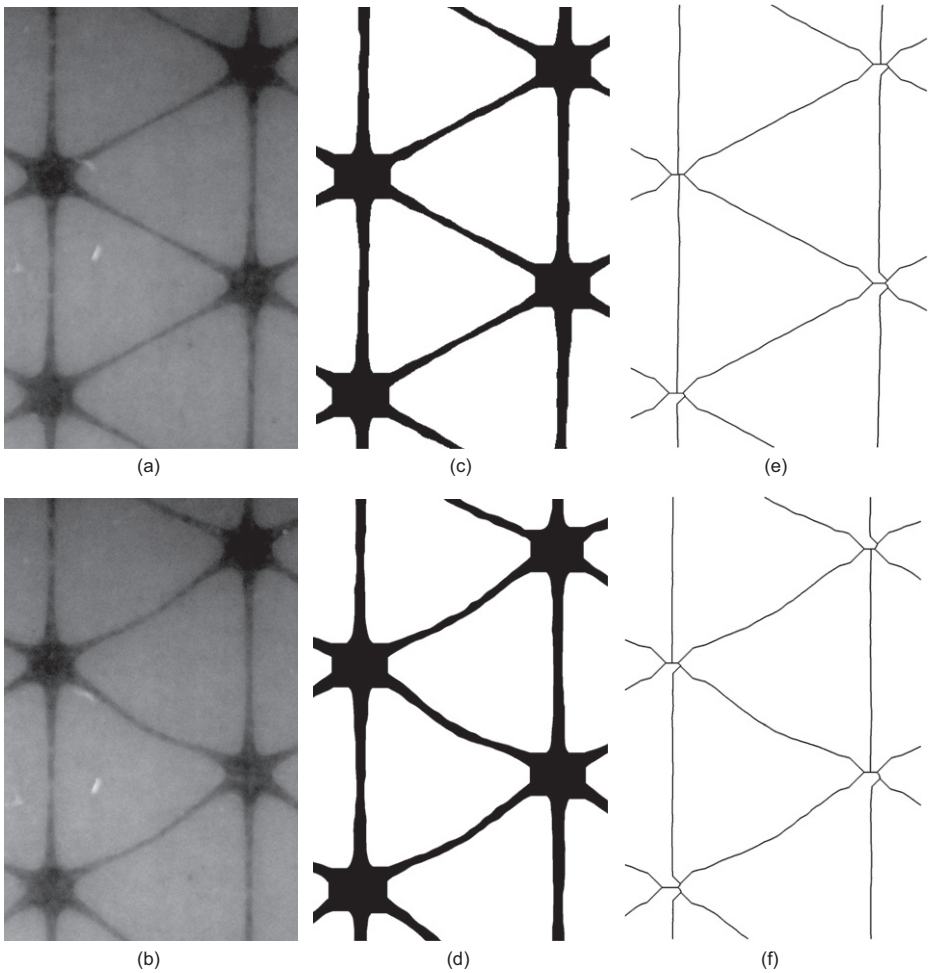

Figure 7. Key steps for topological skeletonization: the cropped greyscale images for (a) undeformed rib-shape and (b) deformed rib-shape, the binarized images for (c) undeformed rib-shape and (d) deformed rib-shape, and the topological skeletons for (e) undeformed rib-shape and (f) deformed rib-shape

G1 are discussed here in detail to illustrate the type of data that could be obtained using the new test setup. The normal stress applied during this test was 27.6 kN/m^2. Frontal and side views of this test, captured separately using Digital Cameras I and II, are shown in Figure 5. The correlation area and corresponding vertical displacement field of the geogrid at the time of pullout failure are displayed in Figures 6a and 6b. The soil displacement field in the laser-illuminated plane was also obtained using DIC techniques. The correlation area and corresponding vertical displacement field of the soil particles at the time of pullout failure are presented in Figures 6c and 6d.

The deflection distribution along each transverse rib of the biaxial geogrid could also be quantified using DIC techniques. As Figure 2 shows, one main difference between biaxial and triaxial geogrids is that triaxial geogrids have smaller rib widths than typical biaxial geogrids. This feature made it difficult to paint white markers on the top surface of the triaxial geogrid ribs and, as a result, DIC techniques did not provide the quality data needed to track the deflection distribution along each diagonal rib. Consequently, topological skeletonization and discretization (TSD) techniques were applied. Figure 7 illustrates the key steps of this image processing method to obtain the deflection profile of a diagonal-rib element of Geogrid G2 at the time of pullout failure.

Since the geometry of the geogrid's diagonal rib elements is essentially symmetrical, a series of image processing techniques were applied to generate the medial axes of the rib elements. Accordingly, the deflection distribution of the diagonal rib elements can be quantified by tracking the shapes of their medial axes.

Figures 7a and 7b show the cropped image frames for undeformed and deformed diagonal rib elements, respectively. Figures 7c and 7d show the binarized images generated by applying a number of image-processing algorithms, including filtering, adjusting global and local brightness and contrast, subtracting background, and binarization. Figures 7e and 7f were obtained by removing pixels from the edges of ribs and junctions in the binarized images until they were reduced to single-pixel-wide shapes. The single-pixel-wide shapes are also referred to as topological skeletons.

After the topological skeletons of the diagonal rib elements have been produced, their deformations were quantified by completing the following three steps: (1) discretizing the topological skeletons with a sequence of points (as shown in Figure 8); (2) locating these points

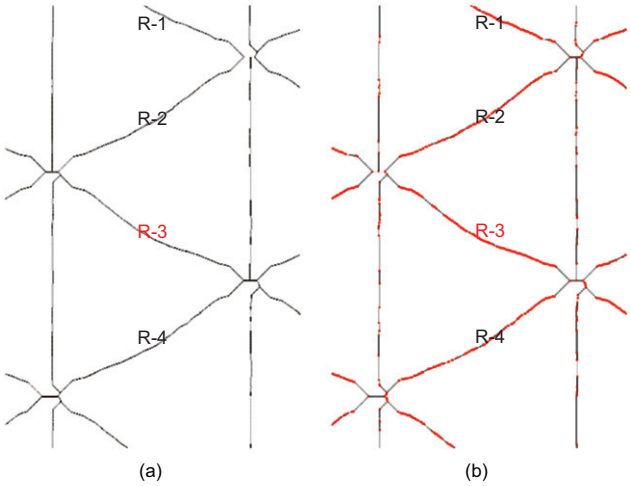

Figure 8. Rib discretization: (a) Topological skeletons of the diagonal-rib elements, and (b) discretized topological skeletons with a sequence of red dots

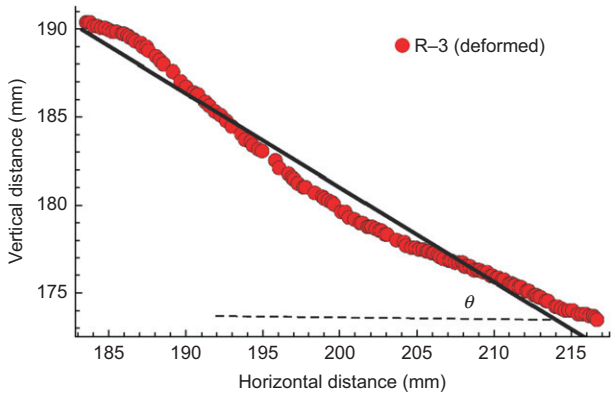

Figure 9. Discretized dots of the topological skeleton of R-3 in the Cartesian coordinate system. θ is the slope angle of the linear fitting line for the red dots from the horizontal direction

in a Cartesian coordinate system (as shown in Figure 9); (3) rotating the discretized diagonal ribs to horizontal (parallel to the x-axis) and shifting the end (the left end, in this case) of the rib to the origin of the Cartesian coordinate system (as shown in Figure 10).

An example of the implementation of these steps for one of the diagonal ribs (R-3 in Figure 8) at the time of pullout failure is illustrated herein. Figure 8a shows a cropped image with topological skeletons; Figure 8b shows the discretization of the topological skeletons with a sequence of red dots. The dots were located in a Cartesian coordinate system based on their pixel locations in the original image, as shown in Figure 9. Figure 10 shows the dot-represented rib-shape after shifting it to the origin of the coordinate system and rotating it at an angle θ (the slope angle of the linear fitting line for the red dots). Figure 11 compares the original undeformed shape of rib R-3 against its deformed shape at the time of pullout failure. As Figure 11 illustrates, the maximum deflection of this rib at the time of pullout failure was about 30.49 pixels, which corresponds to 2.03 mm (1 pixel = 6.67×10^{-2} mm).

The consistency of measurements obtained using different methods was evaluated by calibrating the speeds of

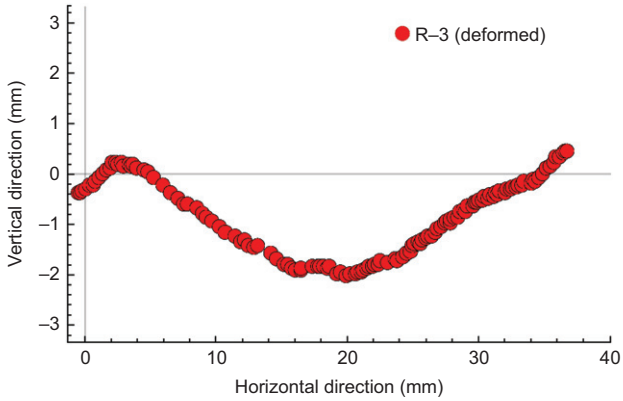

Figure 10. The dot-represented rib-shape of R-3 after shifting and rotating in the Cartesian coordinate system

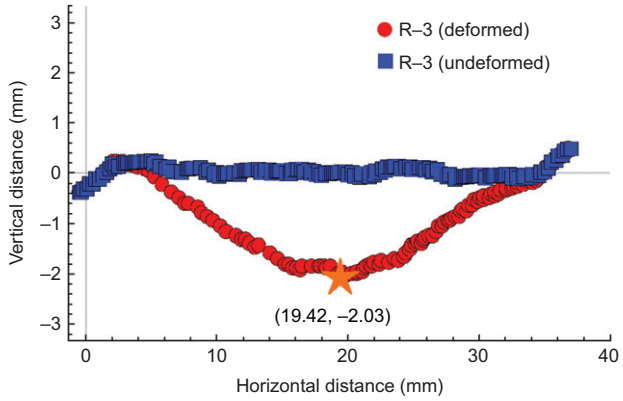

Figure 11. The comparison between the undeformed rib-shape and the deformed rib-shape of R-3 at the time reaching pullout failure

the load frame for different power levels of the loading machine. This calibration process involved two independently conducted series: the first calibration was completed using Linear Variable Differential Transformers (LVDTs) and the second was completed using Digital Camera I. Both DIC and TSD techniques were used to track displacements of the moving head of the load frame. The calibration results displayed in Figure 12 reveal similar linear calibration lines for the three different measuring techniques used, especially for the two image-processing techniques. This indicates that the measurements obtained from the two different image-processing techniques adopted in this study are consistent with traditional physical sensor measurements.

4. EVALUATION OF TYPICAL TEST RESULTS

As discussed in the Introduction, a series of experimental tests, involving the use of more than five types of geogrids with different geometric characteristics, were conducted to evaluate soil-geogrid interaction using geogrids with different geometric characteristics. As also discussed in the previous section, two different image processing techniques were applied to track the rib deflections of

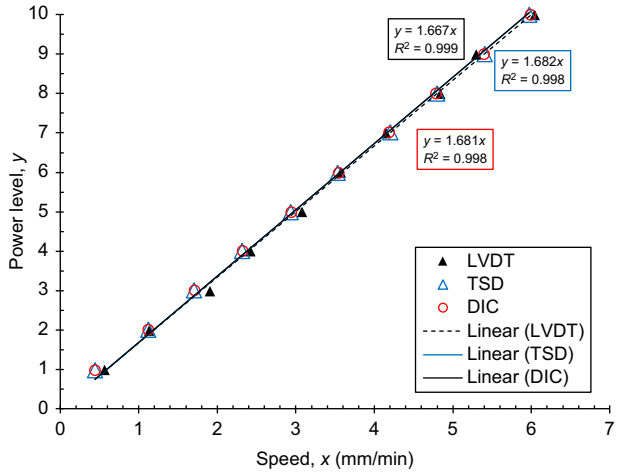

Figure 12. Load frame speed rate calibration using different measuring techniques

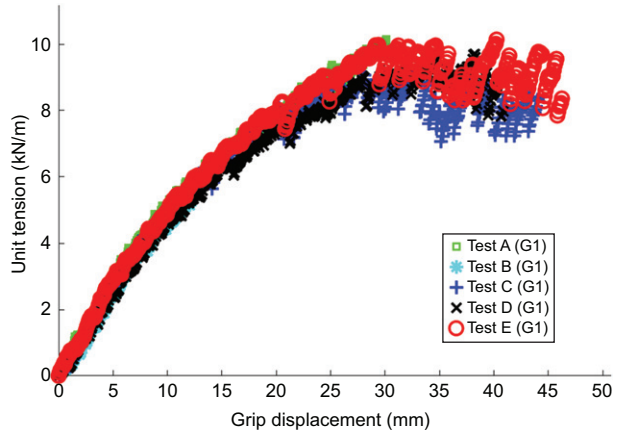

Figure 13. Selected loading curves from the tests conducted using Geogrid G1

Geogrids G1 and G2. In this section, typical test results from a prototype test conducted using Geogrid G1 are presented. A detailed evaluation regarding observations from the results of the experimental tests using different geogrids, including G1, G2 and other geogrid types, is beyond the scope of this paper. Tests involving all the investigated geogrid types showed good repeatability. Figure 13 shows the loading curves obtained from five repeat tests conducted under a confining pressure of 27.6 kN/m^2 using Geogrid G1. The testing configuration for all five tests shown in the figure was the same. As previously discussed, the lengths of the unconfined portion of all geogrid specimens tested were minimized and maintained to be approximately the same among all testing specimens to reduce the effect of the unconfined tensile behavior on the confined performance of the reinforcement. The displacement rate, as defined by the movement of the roller grip of the load frame, was 1 mm/min. The test results presented next to illustrate the type of data generated using the new test setup are those corresponding to Test E in Figure 13.

The relationship between the frontal load (unit tension) and time (grip displacement) is presented in Figure 14.

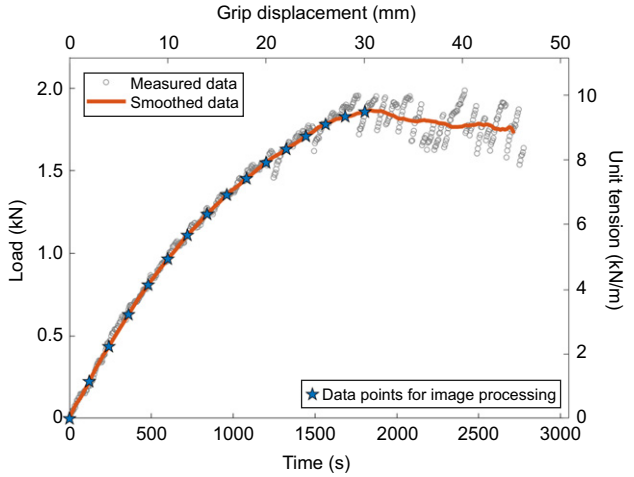

Figure 14. Relationship between frontal load (or unit tension) and time (or grip displacement) during the test conducted using Geogrid G1

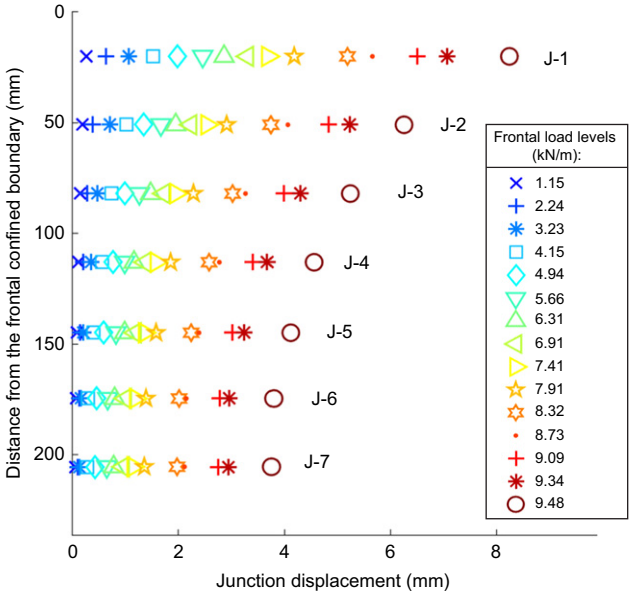

Figure 15. Junction displacement distribution for increasing frontal load levels during the test conducted using Geogrid G1

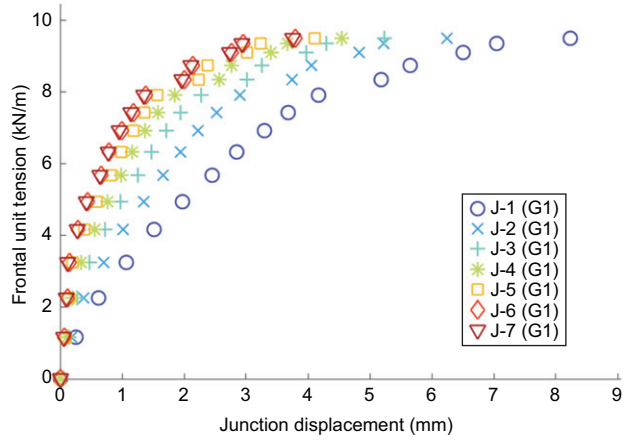

Figure 16. Relationship between the frontal unit tension and the junction displacement during the test conducted using Geogrid G1

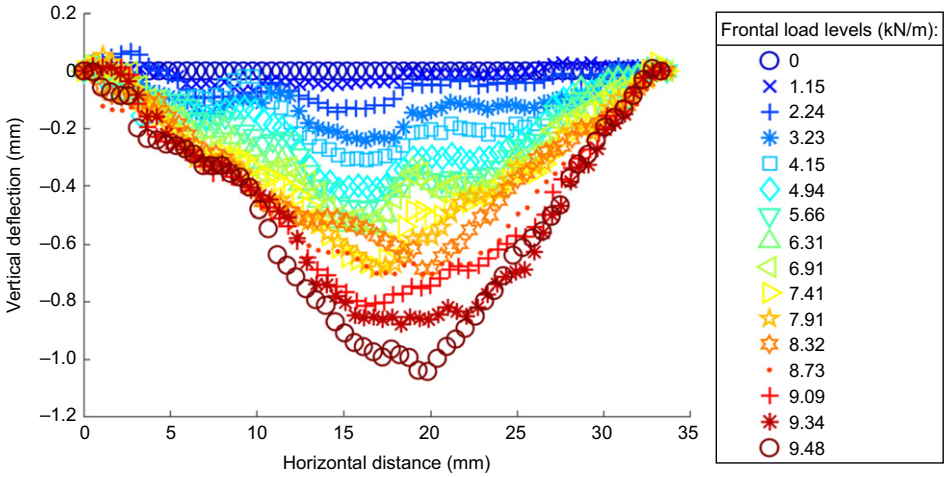

Figure 17. Deflection profiles of a transverse-rib element of Geogrid G1 for increasing frontal load levels measured using DIC techniques

The measured data (grey circles) in the graph in Figure 13 correspond to the measured data (red circles) displayed in Figure 13 for Test E. These measurements were collected by the load cell shown in Figure 3. The moving average method, with a span of 100 data points, was used to smoothen the data (orange curve in Figure 14). The recorded load measurements were normalized by the width of the geogrid specimen used in this test, which was 195.6 mm, to define the 'unit tension'. Sixteen images were selected for image processing. Each image was captured at the time indicated by a blue star in Figure 14 and the average time span between two successive images was about 120 s. The last selected image corresponds to the time of pullout failure. The maximum pullout resistance of Geogrid G1, as measured in this test, was found to be 9.48 kN/m, corresponding to a grip displacement of about 30 mm.

4.1. Measurements of the deformation of geogrid specimens

Displacement distributions of geogrid specimens in the direction of loading for different frontal load levels are relevant data to evaluate the confined performance of geogrids. Due to the orthogonal junction shape of Geogrid G1, the junction nodes with permanent white markers presented more distinct tracking features than the markers located along the longitudinal rib sections. Consequently, the displacement measurements obtained near the junction locations were generally found to be more reliable than those obtained at other locations. To minimize potential boundary effects on data measurements, the junction nodes located at the central two longitudinal ribs were selected for DIC analysis. The average junction displacement distribution along the central two longitudinal ribs is shown in Figure 15 for different frontal load levels. Figure 15 shows the initial location of the first junction node was about 20 mm away from the top frontal boundary, with a movement of about 8 mm. The results also indicate that the junction displacement distribution in the confined portion of Geogrid G1 was nonlinear. The nonlinearity of the displacement

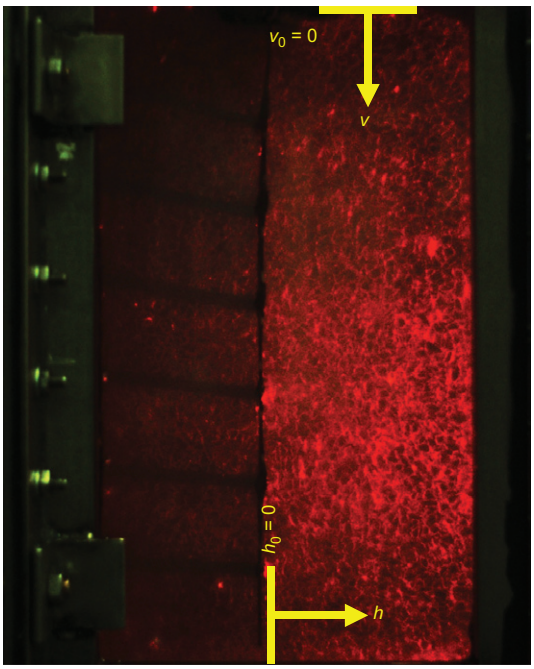

Figure 18. Baselines along the loading (vertical) and the normal (horizontal) directions for evaluating soil displacement mobilization

profile indicates the changing strains in the direction of loading. Considering a case with a similar confining pressure, Ezzein and Bathurst (2014) reported a higher geogrid displacement at the frontal end. This is probably because of different scales of experimental setup and different boundary condition of the rear end of the reinforcement.

Figure 16 shows the relationship between the frontal unit tension and displacement of each junction (J-1 to J-7 in Figure 15). It can be observed that the initial slopes of the load-displacement curves decrease with increasing distance from the frontal confined boundary.

Figure 17 shows the deflection profiles of a transverse-rib element of Geogrid G1, measured using DIC techniques for increasing values of frontal unit tension. Deflection profiles for other transverse-rib elements can

also be obtained and plotted similarly. The measurements of the deflection profiles in both biaxial and triaxial geogrids are expected to lead to the development of load transfer models to predict the resistance contribution from the passive bearing rib components.

4.2. Measurements of the displacement within the soil mass

In the prototype test conducted using Geogrid G1, the laser was shot continuously from the front of the transparent soil model, with a distance of 75 mm between the laser plane and transparent sidewall. To evaluate soil mobilization during the test, several profiles in both loading and normal directions (v and h directions in Figure 18), as presented in Table 4, were selected in the correlation area of the laser-illuminated plane. The unique pattern tracked by the DIC code is the laser-illuminated particle boundaries and some other imperfections both outside and inside the fused quartz particles.

Table 4. Locations of soil displacement profiles in loading (vertical) and normal (horizontal) directions

Profiles in the loading (vertical) direction, distance from geogrid plane, h (mm)	Profiles in the normal (horizontal) direction, distance from frontal confined boundary, v (mm)
0	60
10	100
20	140
40	180

Figure 19 displays the soil displacement distribution along the profiles in the direction of loading (the first column of Table 4) for increasing frontal loads. Soil displacements at the initial locations of all the junctions are displayed as plot markers in Figure 19a.

In the recorded side-view images, one pixel represents 0.12 mm, thus the resolution of the DIC calculation is 0.012 mm (0.1 pixel). Using this relatively high resolution, Figure 19 exhibits the general trends of soil displacement distributions at different frontal load levels. It shows that the crests of the soil displacement profiles are typically located close to the initial locations of the junctions in the direction of loading. This is probably because the junction nodes have a larger depth than the rib elements, which may induce an additional localized shear zone to mobilize surrounding soil particles. Also, the locally mobilized passive bearing resistance generated from the transverse rib elements could further mobilize soil particles in their surrounding area. At the soil-geogrid interface (Figure 19a), the maximum and minimum soil displacements at the time approaching pullout failure were about 5.7 mm and 1.3 mm, respectively. In contrast, Figure 15 indicates that the maximum and minimum junction displacements at the same time were about 8.2 mm and 3.7 mm, respectively. According to the data displayed in Figures 15 and 19a, the trends of the relative displacement profiles at the soil-geogrid interface can be estimated as shown in Figure 20 for increasing load levels. As illustrated by these results, the magnitude of the displacement of soil particles induced by the movement of the geogrid was quite significant. Additionally, the relative displacement profiles show comparatively linear trends for low frontal load levels. This may indicate that

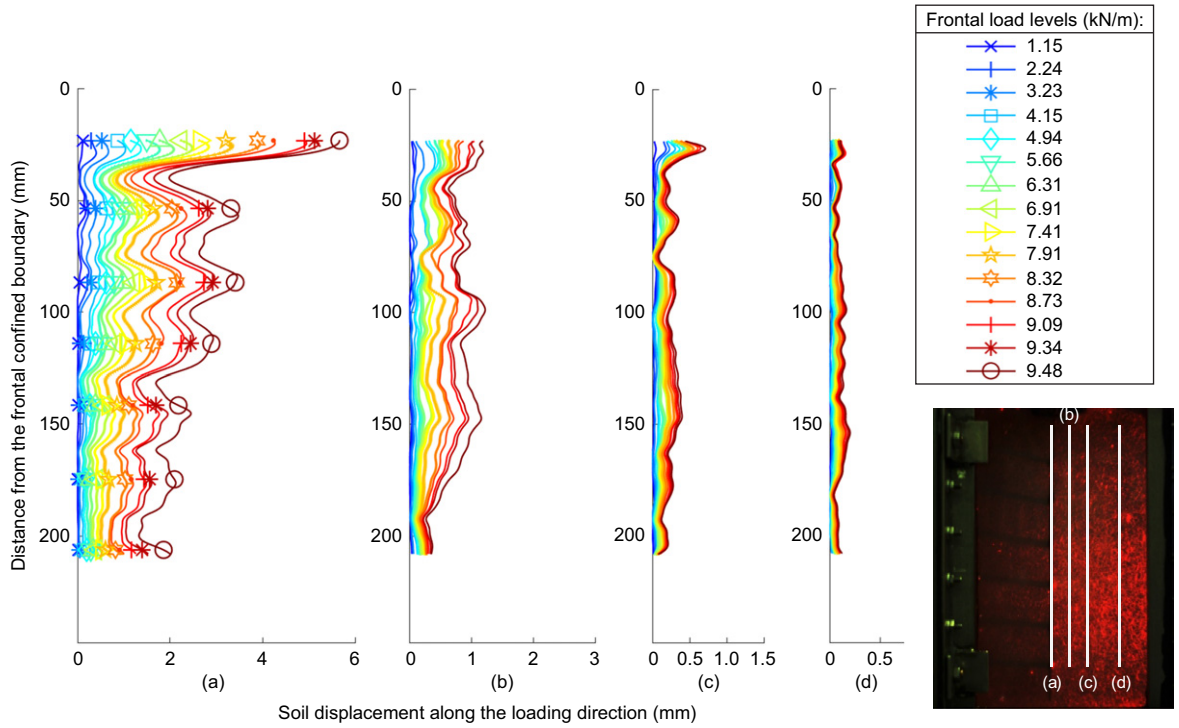

Figure 19. Soil displacement profiles in the direction of loading in the laser-illuminated plane during the test conducted using Geogrid G1: (a) at 0 mm, (b) at 10 mm, (c) at 20 mm, and (d) at 40 mm from the geogrid plane

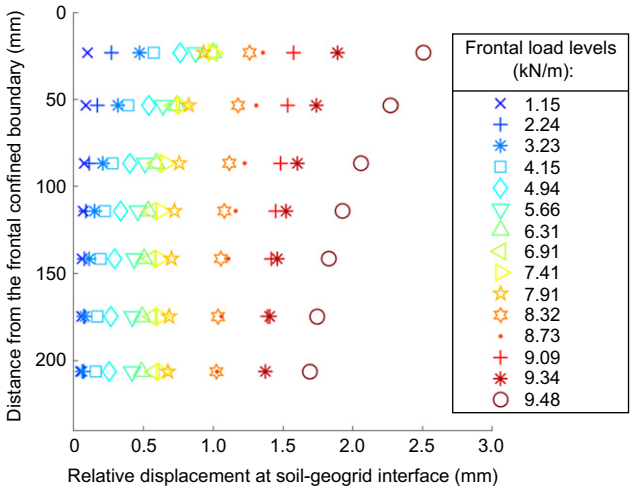

Figure 20. Relative displacement profile at the soil-geogrid interface for increasing frontal load levels during the test conducted using Geogrid G1

only minor strains developed at the soil-geogrid interface. However, the relative displacement profiles show an increasingly significant nonlinearity of the trends with an increase in frontal load levels. This probably represents that an increase in interface strain developed. Even though two different studies have several differences as previously discussed, the nonlinearity of the trends of relative displacement profiles was also reported by Ezzein and Bathurst (2014).

Figure 21 shows the soil displacement distribution along the profiles in the normal direction (the second column of Table 4) for increasing frontal load levels. The results in this figure illustrate relatively smooth shear band profiles at each selected distance from the frontal confined boundary. Evaluation of the results obtained from both Figures 19 and 21 indicate that, for distances beyond 40 mm from the geogrid plane, the soil displacements were always under 0.2 mm, which is about 0.05 times the median size of the granular medium ($D_{50} = 3.9$ mm). Additionally, no significant decrease in soil displacements was observed for distances beyond 40 mm. Overall, the

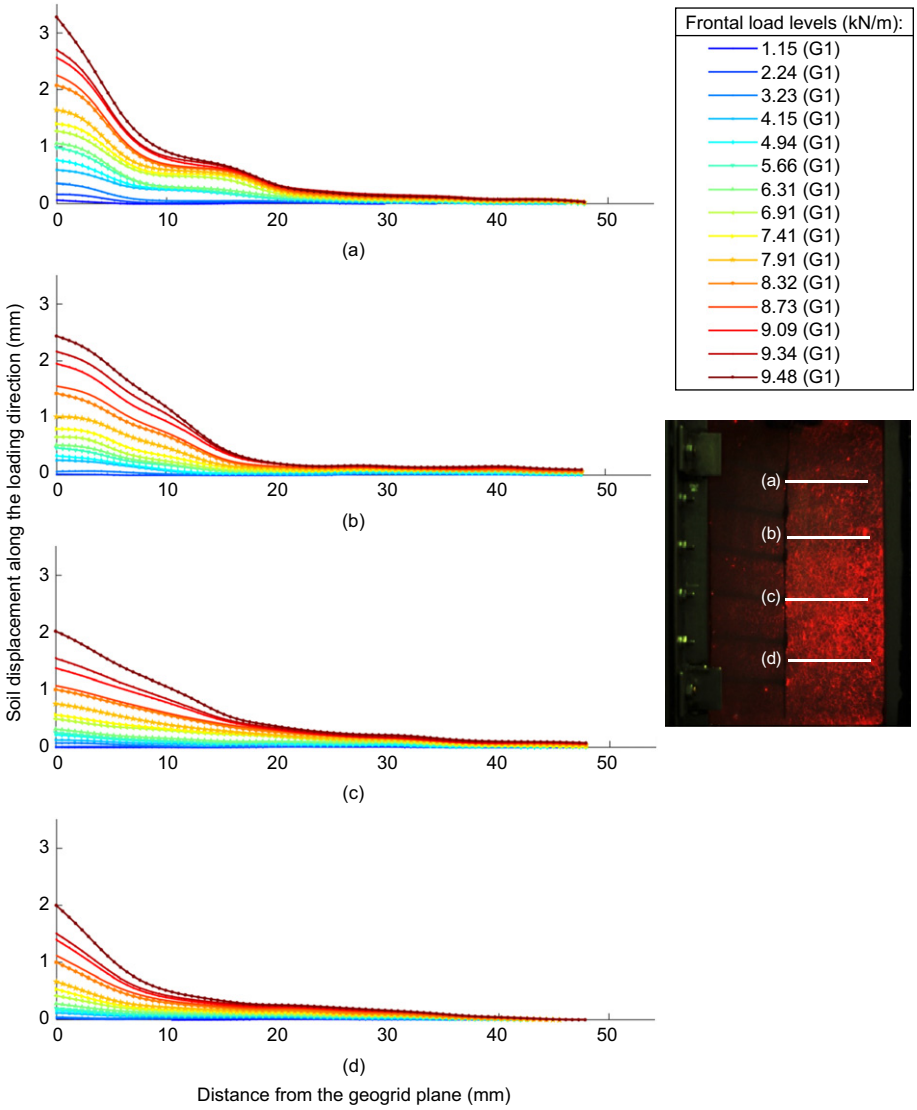

Figure 21. Soil displacement profiles along the normal direction in the laser-illuminated plane during the test conducted using Geogrid G1: (a) profiles at 60 mm, (b) 100 mm, (c) 140 mm, and (d) 180 mm from the frontal confined boundary

shapes of shear band profiles are a direct reflection of the load transfer mechanisms between soil particles and geogrid specimens. Thus, it should be expected that geogrids with different geometric characteristics would develop different shapes of shear band profiles, even at similar frontal load levels.

5. SUMMARY AND CONCLUSION

In this study, a new experimental approach involving the use of transparent soil with laser-aided imaging was developed and found to capture the deformations of both geogrid specimens and soil particles non-intrusively and adequately. Specifically, the use of transparent soil facilitated visualization of the deformation of confined geogrid specimens. Laser beams with output power up to 350 mW and a wavelength of 638 nm were implemented to track the transparent soil particles at a plane perpendicular to the soil-geogrid interface. The collimated beam produced well-defined individual particles in the selected plane of the soil model. Digital cameras were used to track the displacement fields of the confined geogrid specimen and soil particles within the laser-illuminated plane.

DIC and TSD were proved to be adequate techniques to process the data, allowing quantification of the displacements in the geogrid elements and the soil particles. Digital image techniques that are best suited for analysis were found to depend on the specific geometry of the geogrid. Specifically, DIC techniques (involving painted patterns) and TSD techniques were found to be adequate to quantify the deflection profiles in biaxial and triaxial geogrids respectively, with a relatively high resolution. These measurements are expected to lead to the development of load transfer models to predict the resistance contribution from the passive bearing rib components.

DIC analysis was found to define the displacement fields of soil particles in the laser-illuminated plane adequately. Consequently, soil displacement profiles in the direction of loading could be quantified for increasing frontal load levels. Additionally, the development of shear band profiles in the soil were quantified using DIC techniques. The non-intrusive methods of measurement applied in this study highlight the feasibility of and need for further evaluation of the load-transfer mechanisms of geogrids with different geometric characteristics.

ACKNOWLEDGEMENTS

The researchers gratefully acknowledge the funding provided by the Tensar Corporation to conduct this experimental study. The continued technical support provided by M. Wayne of the Tensar Corporation and J. Friedrichsen of National Instruments (NI) is also gratefully acknowledged.

REFERENCES

Abu-Farsakh, M. Y. & Chen, Q. (2011). Evaluation of geogrid base reinforcement in flexible pavement using cyclic plate load testing. *International Journal of Pavement Engineering*, **12**, No. 3, 275–288.

Alagiyawanna, A. M. N., Sugimoto, M., Sato, S. & Toyota, H. (2001). Influence of longitudinal and transverse members on geogrid pullout behavior during deformation. *Geotextiles and Geomembranes*, **19**, No. 8, 483–507.

ASTM D3080/D3080M-11 *Standard Test Method for Direct Shear Test of Soils Under Consolidated Drained Conditions*. ASTM International, West Conshohocken, PA, USA.

ASTM D854-14 *Standard Test Methods for Specific Gravity of Soil Solids by Water Pycnometer*. ASTM International, West Conshohocken, PA, USA.

ASTM D4253-16 *Standard Test Methods for Maximum Index Density and Unit Weight of Soils Using a Vibratory Table*. ASTM International, West Conshohocken, PA, USA.

ASTM D4254-16 *Standard Test Methods for Minimum Index Density and Unit Weight of Soils and Calculation of Relative Density*. ASTM International, West Conshohocken, PA, USA.

Bathurst, R. J. & Ezzein, F. M. (2016). Geogrid pullout load–strain behaviour and modelling using a transparent granular soil. *Geosynthetics International*, **23**, No. 4, 271–286.

Bathurst, R. J. & Ezzein, F. M. (2017). Insights into geogrid–soil interaction using a transparent granular soil. *Géotechnique Letters*, **7**, No. 2, 179–183.

Black, J. A. (2015). Centrifuge modelling with transparent soil and laser aided imaging. *Geotechnical Testing Journal*, **38**, No. 5, 631–644.

Chen, Q., Abu-Farsakh, M. & Tao, M. (2009). Laboratory evaluation of geogrid base reinforcement and corresponding instrumentation program. *ASTM Geotechnical Testing Journal*, **32**, No. 6, 516–525.

Chini, C. M., Wallace, J. F., Rutherford, C. J. & Peschel, J. M. (2015). Shearing failure visualization via particle tracking in soft clay using a transparent soil. *Geotechnical Testing Journal*, **38**, No. 5, 708–724.

Collin, J. G., Kinney, T. C. & Fu, X. (1996). Full scale highway load test of flexible pavement systems with geogrid reinforced base courses. *Geosynthetics International*, **3**, No. 4, 537–549.

Ezzein, F. M. & Bathurst, R. J. (2011). A transparent sand for geotechnical laboratory modeling. *ASTM Geotechnical Testing Journal*, **34**, No. 6, 590–601.

Ezzein, F. M. & Bathurst, R. J. (2014). A new approach to evaluate soil-geosynthetic interaction using a novel pullout test apparatus and transparent granular soil. *Geotextiles and Geomembranes*, **42**, No. 3, 246–255.

Ferreira, J. A. Z. (2013). *Evaluation of Soil-Geogrid Interaction at Different Load Levels Using Pullout Tests and Transparent Soil*, PhD dissertation, University of Texas at Austin, Austin, TX, USA.

Ferreira, J. A. & Zornberg, J. G. (2015). A transparent pullout testing device for 3D evaluation of soil–geogrid interaction. *Geotechnical Testing Journal*, **38**, No. 5, 686–707.

Iskander, M. (2010). *Modelling with Transparent Soils: Visualizing Soil Structure Interaction and Multi Phase Flow, Non-Intrusively*, Springer-Verlag, Berlin, Heidelberg, Germany.

Jones, E. (2014). *DIC Challenge – Summary of Results*, University of Illinois at Urbana-Champaign, Champaign, IL, USA.

Jones, E. (2015). *Documentation for Matlab-Based DIC Code, Version 4*, University of Illinois at Urbana-Champaign, Champaign, IL, USA.

Koerner, R. M. (2012). *Designing with Geosynthetics*, 6th edn, Xlibris Corporation.

Ochiai, H., Otani, J., Hayashic, S. & Hirai, T. (1996). The pull-out resistance of geogrids in reinforced soil. *Geotextiles and Geomembranes*, **14**, No. 1, 19–42.

Otani, J., Mukunoki, T. & Obara, Y. (2000). Application of X-ray CT method for characterization of failure in soils. *Soils and Foundations*, **40**, No. 2, 111–118.

Peng, X. & Zornberg, J. G. (2017). Evaluation of load transfer in geogrids for base stabilization using transparent soil. *Procedia Engineering*, **189**, 307–314.

Roodi, G. H. & Zornberg, J. G. (2017). Stiffness of soil-geosynthetic composite under small displacements. II: experimental evaluation. *Journal of Geotechnical and Geoenvironmental Engineering*, **143**, No. 10, 04017076.

Sieira, A. C. C., Gerscovich, D. M. & Sayao, A. S. (2009). Displacement and load transfer mechanisms of geogrids under pullout condition. *Geotextiles and Geomembranes*, **27**, No. 4, 241–253.

Teixeira, S. H., Bueno, B. S. & Zornberg, J. G. (2007). Pullout resistance of individual longitudinal and transverse geogrid ribs. *Journal of Geotechnical and Geoenvironmental Engineering*, **133**, No. 1, 37–50.

Tran, V. D. H., Meguid, M. A. & Chouinard, L. E. (2013). A finite–discrete element framework for the 3D modeling of geogrid–soil interaction under pullout loading conditions. *Geotextiles and Geomembranes*, **37**, 1–9.

Wang, Z., Jacobs, F. & Ziegler, M. (2016). Experimental and DEM investigation of geogrid–soil interaction under pullout loads. *Geotextiles and Geomembranes*, **44**, No. 3, 230–246.

White, D. J. (2002). *Investigation Into the Behaviour of Pressed-in Piles*. PhD dissertation, University of Cambridge, Cambridge, UK.

White, D. J., Take, W. A. & Bolton, M. D. (2003). Soil deformation measurement using particle image velocimetry (PIV) and photogrammetry. *Geotechnique*, **53**, No. 7, 619–632.

Wilson-Fahmy, R. F. & Koerner, R. M. (1993). Finite element modelling of soil-geogrid interaction with application to the behavior of geogrids in a pullout loading condition. *Geotextiles and Geomembranes*, **12**, No. 5, 479–501.

Ziegler, M. & Timmers, V. (2004). A new approach to design geogrid reinforcement. In *Proceedings of the 3rd European Geosynthetics Conference*, Geotechnical Engineering with Geosynthetics, Zentrum Geotechnik, Munich, Germany, pp. 661–666.

Zornberg, J. G., Sitar, N. & Mitchell, J. K. (1998). Performance of geosynthetic reinforced slopes at failure. *Journal of Geotechnical and Geoenvironmental Engineering*, **124**, No. 8, 670–683.

The Editor welcomes discussion on all papers published in Geosynthetics International. Please email your contribution to discussion@geosynthetics-international.com by 15 October 2019.